Coaxial Rotor CFD Validation and ML Surrogate Model Generation

Jason Cornelius
Aerospace Engineer
NASA Ames Research Center
Moffett Field, CA, 94035, USA

Sven Schmitz
Boeing/A.D. Welliver Professor
The Pennsylvania State University
University Park, PA, 16802, USA

ABSTRACT

A fixed-pitch speed-controlled coaxial rotor system was tested in the NASA Langley Transonic Dynamics Tunnel in September 2022. The rotors have a diameter of 1.35 meters and an inter-rotor spacing of 25% of the diameter. Though this test was focused on the NASA New Frontiers Dragonfly mission, the resulting dataset is relevant to a wide array of applications of multirotor vehicles, especially those using fixed-pitch variable-speed rotors. Most notably beyond Dragonfly, perhaps, is the application of coaxial rotor pair configurations for eVTOL and Urban Air Mobility (UAM) aircraft. This work provides a thorough CFD validation study quantifying coaxial rotor performance estimation with accuracy on order 5-10% using an efficient hybrid BEMT-URANS flow solver over a wide range of operating conditions. This accuracy was achieved using novel approaches for the construction of both the C81 airfoil performance lookup tables and the BEMT rotor model. These novel approaches are combined with advanced scripting to further accelerate the commercial off-the-shelf CFD solver on GPU accelerated machines. Finally, the development of machine learning surrogate models is presented to produce highly efficient and accurate rotor performance predictions for fixed-pitch variable-speed multirotor aircraft over the complete flight regime including scout, cruise, climb, descent, as well as limiting cases of vortex-ring and windmill-brake states.

NOTATION

A	Rotor Disk Area [m^2]
C_T	Thrust Coefficient $C_T = T/(\rho A \Omega^2 R^2)$
C_Q	Torque Coefficient $C_Q = Q/(\rho A \Omega^2 R^3)$
D	Rotor Diameter [m]
P	Rotor Power [W]
Q	Rotor Torque [Nm]
R	Rotor Blade Radius [m] $R = 0.5D$
r	Radial Location [m]
S	Inter-rotor Spacing [%D]
SA	Shaft Angle, [deg]
T	Rotor Thrust [N]
Ω	Rotor Speed, [Rad/s]
ρ	Fluid Density [kg/m^3]
V	Flight Speed [m/s]
V_x	Rotor Edgewise Speed[m/s] $V_x = V\cos(SA)$
V_z	Rotor Axial Speed [m/s] $V_z = -V\sin(SA)$
v_h	Equivalent Hover Induced Velocity [m/s] $v_h = \sqrt{T/(2\rho A)}$
μ_x	Edgewise Advance Ratio $\mu_x = V_x/\Omega R$
μ_z [λ]	Axial Inflow Ratio $\mu_z = V_z/\Omega R$

INTRODUCTION

Applications and use cases for multirotor aircraft have been rapidly expanding in the last several years. This increase in use has been driven by innovation in lightweight structures, distributed electric propulsion, and advanced control systems that can orchestrate the control of multiple rotors in a system to attain the desired vehicle performance. These multirotor vehicles largely started in the recreational hobby market with remote control drones but have since expanded to be used in various other sectors such as commercial, military, and even space exploration.

Various multirotor vehicle configurations have been proposed (and built) for commercial activities such as adding capability to an electrician inspecting power lines, a farmer tending his fields, package delivery, or emergency response, Refs. [1-4]. On the military side, drones have been built that fit in a soldier's pocket for reconnaissance as well as larger ones deployed from the back of a ground vehicle to deliver fuel and other supplies quickly to a hostile location. Personal transport, which may be a sub-category within the commercial industry, has seen rapid growth in the number of designs proposed for on-demand mobility, Refs. [5-6]. The Vertical Flight Society has documented close to one thousand electric and hybrid-electric Vertical Take-off and Landing (eVTOL) concepts,

Presented at the VFS 6th Decennial Aeromechanics Specialists' Conference, Santa Clara, CA, USA Feb.6-8, 2024.

Ref. [7]. Many of these vehicles are being proposed to deliver passengers quickly from one location to another in an urban environment. The takeaway is that multirotor aircraft (large or small, uninhabited or passenger-carrying) are poised to make broad impacts on a variety of aviation-sector applications in the coming years.

The above examples and applications are akin to conventional rotorcraft design in that the vehicles take-off and land vertically, but beyond that similarity, there are many stark differences in the way these vehicles are designed, built, and operated. The largest differentiator between conventional helicopter design and this new set of vertical flight vehicles is their vehicle control methodology. Many conventional rotorcraft rely on fully-articulated rotor systems and the implementation of collective and cyclic rotor control to attain a desired control state of the vehicle. Many of these new configurations, however, leverage their multirotor layout with distributed electric propulsion to control the vehicle via independent actuation of each rotor's speed. This allows these multirotor vehicles to be designed with reduced complexity of their rotor systems, which explains fixed-pitch rotors being used by a large majority of the configurations.

There are of course some configurations from both the conventional rotorcraft and the multirotor categories that differ from the 'general' design methodology, which make use of hybrid approaches and technologies. Still, the growth of the multirotor market into several additional sectors has prompted a desire for further design and analysis methods to create and improve these vehicles. This has led to increased demand for better computational tools and approaches that analyze and predict their performance. NASA is one such example having recently added an Advanced Air Mobility (AAM) Mission Integration Office to its Aeronautics Research Mission Directorate (ARMD). The office has contributing projects from AAM, Revolutionary Vertical Lift Technology (RVLT), and Transformational Tools and Technologies (TTT), among others, as illustrated in Fig. 1 reproduced from Ref. [8].

Figure 1. NASA Advanced Air Mobility National Campaign, Ref. [8].

This paper first presents background information on multirotor vehicles followed by the development of methodologies supporting their modeling. Comparisons of model results to recently obtained multirotor experimental data are made. A more detailed description of the methodologies presented in this paper is available in Ref. [9].

BACKGROUND

The analyses presented throughout this work pertain to a growing subset of fixed-pitch multirotor systems i.e., small-scale (less than 2-meter diameter), stiff (1st flap frequency > 1.5/Rev), RPM-controlled (variable-speed), and having large rotor separation (separation > D/5) for the coaxial configuration. This blade stiffness is higher, and rotor spacing larger, than typically analyzed for conventional helicopter design and can be representative of some electric vertical take-off and landing (eVTOL) and urban air mobility (UAM) configurations. Much work has been carried out by Silva and Johnson, Refs. [5, 10-13], to develop NASA reference vehicles to support the increase in interest for developing these types of vehicles. Some of the NASA reference vehicles have designs similar to conventional rotorcraft, but many of them are more typical of the rotor configurations discussed in this work. Additionally, Refs. [14-16] provide some recent testing and analysis of multirotor aircraft. Prior work has also applied state-of-the-art computational analysis techniques based on Computational Fluid Dynamics (CFD) to advanced vertical-flight aircraft design and analysis tools, Refs. [17-20].

These multirotor systems are also being used for space exploration of other celestial bodies such as Mars and Titan. The successful flight of the Mars Ingenuity Helicopter, Fig. 2, in April 2021 marked the first flight of a heavier-than-air vehicle on another planet, Refs. [21-24]. Notably, the same CFD solver that will be discussed in this work, RotCFD, was also used in the Ingenuity development effort, Ref. [25]. The Dragonfly lander, Fig. 3, is now the second multirotor vehicle under development to be sent into space following in Ingenuity's footsteps, Ref. [26]. Notably, Dragonfly uses a fixed-pitch variable-speed multirotor configuration for the vehicle's control strategy. Dragonfly is the fourth NASA New Frontiers program with a scientific mission to explore Titan's prebiotic chemistry and habitability. Additional relevant Dragonfly program publications cover topics of conceptual design, blade-tip vortex condensation, entry descent and landing (referred to as transition to powered flight), and the mission's scientific goals that require a relocatable lander, Refs [27-31].

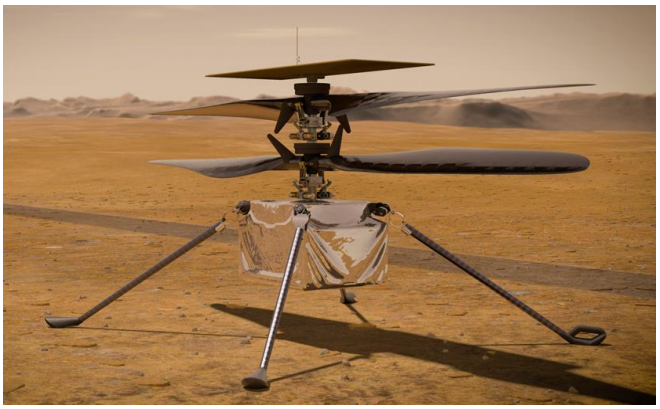

Figure 2. Ingenuity Helicopter, Ref. [32].

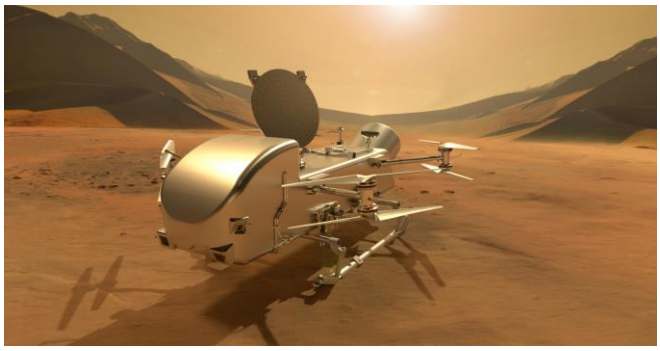

Figure 3. Dragonfly Relocatable Lander, Ref. [33].

It is also noteworthy that NASA Ames has a long history, reaching back twenty-five years or more, of key research and advocacy into both vertical-lift planetary aerial vehicles as well as novel multirotor configurations for a broad range of applications, Refs. [34-47].

Much work remains to improve the understanding and analysis capabilities for these multirotor aircraft often using stiff and RPM-controlled rotors. Many of the new configurations considered today, whether for flight here on Earth or for planetary exploration, make use of this multirotor configuration. A few more examples of vehicles currently under development that use multirotor technology and distributed electric propulsion are included in Fig. 4. The potential applications for these vehicles are continually increasing and the demand for improving their operation will also continue to increase accordingly. Though there are relatively few terrestrial multirotor configurations using coaxial pairs, foundational aerodynamics experimentation and analysis is still an important endeavor. Past studies involving conventional coaxial rotorcraft applications have been summarized by Coleman et al., Ref. [48]. Although these multirotor aircraft can be designed and analyzed with conventional rotorcraft design tools, their novel design aspects create opportunities for improved methods specific to these vehicles. This work summarizes recent efforts to efficiently analyze the performance and aid the design of these multirotor aircraft.

Figure 4. Example Multirotor Aircraft Under Development (starting top-left, then clockwise): Joby S4, Vertical Aerospace VX4, Airbus CityAirbus, and Volocopter VoloCity, Ref. [49].

NASA LANGLEY COAXIAL ROTOR TEST

A fixed-pitch speed-controlled coaxial rotor system was tested in the NASA Langley Transonic Dynamics Tunnel (TDT) in September, 2022, Ref. [50]. This TDT test was one in a series of wind tunnel tests supporting the NASA New Frontiers Mission Dragonfly, which uses a coaxial quadrotor configuration, Refs. [30, 51-55]. An image of the coaxial rotor test assembly is included in Fig. 5. The rotors have a diameter of 1.35 meters and an inter-rotor spacing of 0.3375 meters, or D/4. Though this test was specifically focused on Dragonfly's coaxial rotor system, the results from this test are relevant to a wide variety of multirotor vehicles, especially those using fixed-pitch variable-speed coaxial rotors. This configuration is relevant to the various applications of multirotor vehicles discussed throughout this work. Most notably, perhaps, is the application of this configuration to eVTOL aircraft and UAM. The next section provides a thorough CFD validation study for coaxial rotor performance estimation with accuracy on order 5-10%. This accuracy was achieved using novel rotor modeling approaches for fixed-pitch variable-speed rotors.

Rotor data was obtained at 2kHz with a maximum rotor speed of 1100 RPM. A single six-axis load cell was located under each motor to record individual rotor force and moments. A quarter-second moving average was applied to clean up the raw data. Further averaging of those samples was used to obtain the quasi-steady mean rotor forces and moments. Additional details on the experimental test setup and post-processing can be found in Ref. [52].

Figure 5. Fixed-Pitch Speed-Controlled Coaxial Rotor System in the NASA Langley Transonic Dynamics Tunnel, Ref. [50].

This coaxial rotor system was tested for a wide range of flight conditions from axial climb through edgewise flight and axial descent. A large range of wind tunnel test conditions were used to obtain experimental measurements in all four rotor aerodynamic flow states: 1) normal operation, 2) vortex ring state (VRS), 3) turbulent wake state (TWS), and 4) windmill brake state (WBS). The experimental data are later compared against CFD data for the purposes of validating the CFD model for coaxial rotor performance analysis. The breadth of test conditions is another reason why this wind tunnel test is

a singular rotorcraft experimental database. A subset of comparisons will be shown and discussed to give a brief assessment of the tool's predictive capability in various relevant flight regimes.

The experiment tested the full range of rotor shaft angles from -90 deg (axial climb) through +90 deg (axial descent) in increments of 15 degrees or less. The rotor speed was swept from 430-1100 RPM. Two different wind tunnel velocities were used since testing was conducted in both R134-a heavy gas and air. Due to the higher sectional Reynolds number achieved in R134-a, and the resulting applicability to larger UAM vehicles, the CFD validation will focus on the heavy gas test data that ranged from 2.25 to 12 m/s tunnel speeds. The air data, which is used in the machine learning section along with the heavy gas data, had a wind tunnel velocity range from 4.7 to 21.9 m/s. This test matrix represents the full possible flight envelope for this particular fixed-pitch RPM controlled UAM vehicle, including shallow and steep climbs and descents, hover, cruise, VRS, and WBS. Some experimental data are omitted for conditions that resulted in negative motor power or excessively high test stand vibratory loads.

ROTORCRAFT CFD MODELING

Figure 6 summarizes several approaches that could be used to create a multirotor performance data set, and is re-produced from Cornelius, Schmitz, and Kinzel, Ref. [53].

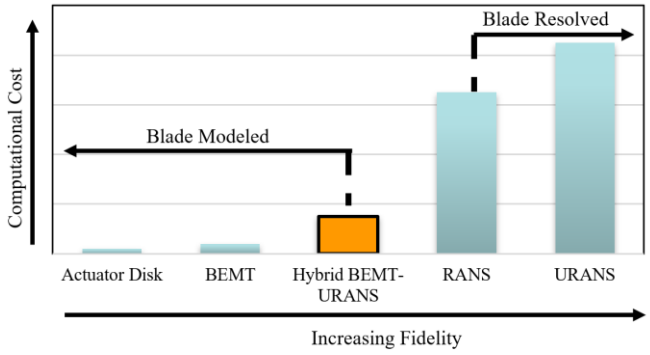

Figure 6. Computational Cost vs. Model Fidelity for Various Rotor Analysis Approaches, Reproduced from Ref. [53].

The state-of-the-art approaches are on the right side of the chart with the highest fidelity and the highest computational cost. On the left side are the blade-modeled approaches, which are much faster but of a lower fidelity. The hybrid Blade Element Momentum Theory with Unsteady Reynolds-Averaged Navier-Stokes (BEMT-URANS) methodology, highlighted orange in the middle of the chart, combines the speed of a blade-modeled approach with the improved accuracy of a URANS CFD resolved inflow and wake. This provides a computational cost somewhere in-between the low- and high-fidelity methods due to its blade-modeled description of the rotor. For time-averaged rotor performance metrics such as thrust, torque, roll moment, and pitching moment, this method provides accuracy comparable with the higher-fidelity methods. Although the blade-resolved models can provide more accurate information in the form of a time-accurate solution, a very carefully constructed model of the rotor blade and its cross-sectional (two-dimensional) airfoil performance can provide very accurate results for the time-averaged values relevant to the flight control system and vehicle conceptual and preliminary design. As such, a hybrid BEMT-URANS multirotor approach, coaxial in this work, is used to efficiently create the CFD rotor performance datasets.

THE ROTCFD HYBRID BEMT-URANS SOLVER

The CFD toolset Rotorcraft CFD (RotCFD) is used in this work to implement the hybrid BEMT-URANS methodology. RotCFD is a self-contained program with provisions for the entire workflow from geometry creation through CFD solution and visualization of the results, Refs. [56-59]. RotCFD uses discretized momentum sources to interface the BEMT rotor module with a finite-volume unstructured Cartesian grid system. Implicit time integration is used to solve the incompressible URANS equations with a two-equation k-ϵ turbulence closure and the SIMPLE-based solution method, Ref. [60]. One of the main benefits of this hybrid BEMT-URANS methodology is that it enables multirotor CFD simulations to be massively parallelized on graphical processing units (GPUs) while still retaining a high level of accuracy for steady rotor performance predictions. This minimizes the time needed to create a training dataset of adequate size and accuracy for the objectives of this work on order thousands of flight conditions and accuracy of 5-10% for rotor thrust and power, Ref. [9].

A RotCFD model was created based on the actual coaxial rotor system tested at the NASA Langley Research Center, depicted in Figure 5. Figure 7 shows the CAD geometry that was used in RotCFD. It includes the coaxial rotor system as well as approximate shapes for the motors, load cells, and sting arm. Modeling these test stand features, in addition to the rotor modeling, was found to be important for successful correlation with the test results.

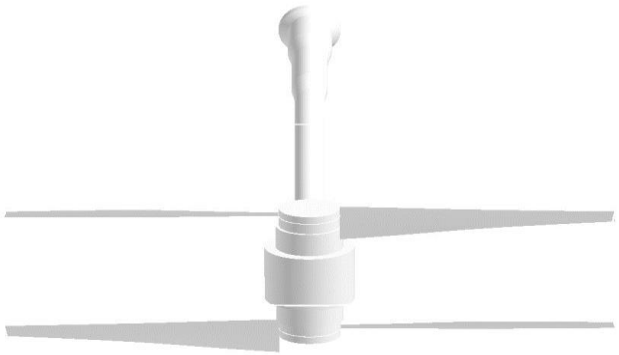

Figure 7. RotCFD Model of the TDT Test.

Since RotCFD is a blade-modeled approach, it uses C81 airfoil performance look-up tables to calculate the momentum source terms in the Cartesian grid system based on the local flow-field around the rotor. For this work, the OVERFLOW solver was used to generate airfoil performance data as a function of airfoil, Mach number, Reynolds number, and angle-of-attack. The wrapper AFTGen, Ref. [61], was used to run the OVERFLOW solver for airfoil performance predictions. AFTGen has a user-friendly graphical user interface with multiple compatible solvers including OVERFLOW, ARC2D, XFOIL, and MSES. Past studies have used C81 tables derived from XFOIL and ARC2D, Ref. [51], but best practices with RotCFD have evolved to now using the OVERFLOW solver.

One of the key aspects to building an accurate hybrid BEMT-URANS CFD model is the creation of high-accuracy and high-discretization C81 tables. As such, the rotor blade was discretized into 13 radial stations from blade root to tip. Each of the 13 stations was simulated in OVERFLOW from -20 deg angle-of-attack to +20 deg. This sweep was simulated at various Mach and Reynolds number combinations, which captures the changing airfoil section performance with changing rotor speed. The full C81 airfoil performance deck for this rotor uses approximately 3,000 OVERFLOW simulations, which were scripted to be massively parallelized on the NASA High-End Compute Capability (i.e. the NASA supercomputers). Airfoil input decks were generated for both the R134-a heavy gas and air test environments, which represents approximately 6,000 distinct OVERFLOW airfoil calculations.

An example image of the RotCFD coaxial rotor model's Cartesian grid system is shown in Fig. 8. Grid convergence studies were carried out to ensure the grid was sufficiently refined. These efforts continue to find that approximately 90 cells across the rotor diameter is ideal for these hybrid BEMT-URANS simulations. This number is also in agreement with other similar past efforts by Koning, Ref [62].

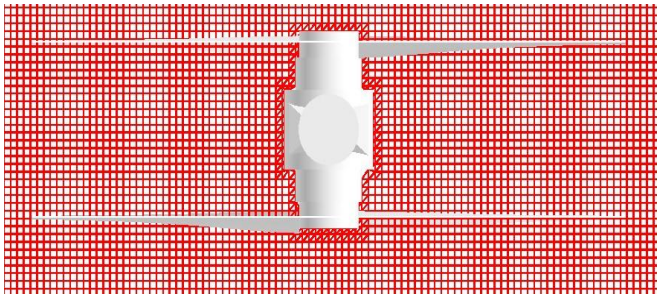

Figure 8. RotCFD Coaxial Rotor Model Grid.

PARALLELIZATION OF THE MODEL ON THE NASA PLEIADES SUPERCOMPUTER

Although the standard RotCFD program is capable of GPU acceleration using the Open Compute Language (OpenCL) architecture, Cornelius and Schmitz recently documented a further parallelization of the hybrid BEMT-URANS solver, Ref. [63]. The optimized GPU scripting achieved a 41-times speedup. This scripting was modified and extended to run on the NASA Pleiades supercomputer, enabling more than a thousand coaxial rotor CFD simulations to be run for this work. In total, 1,970 hybrid BEMT-URANS coaxial rotor simulations were completed. The coaxial dataset has 930 distinct conditions between air and R134-a heavy gas. The single rotor dataset has 520 distinct conditions with each being simulated for both the upper rotor alone and lower rotor alone configurations.

The computational time required for the same model discussed in this work was recently documented, Ref. [63]. The off-the-shelf program running OpenCL on a Nvidia RTX 3090 GPU can reach convergence for the model discussed here in approximately 11.2 hours. The advanced scripting and GPU bash parallelization across the multi-GPU machine described in Ref. [63] reduces the time required per simulation to approximately sixteen minutes.

RESULTS

This section provides a validation study for the hybrid BEMT-URANS coaxial rotor model. The study focuses on validating coaxial rotor performance under R134-a heavy gas conditions. A small subset of the CFD and experimental data will be compared to show the agreement at various relevant portions of the flight envelope to UAM aircraft. Following the CFD model validation study, the generation of machine learning surrogate models using these CFD training datasets is presented and discussed.

CFD VALIDATION

This section documents the comparisons with CFD co-plotted against the experimental data with uncertainty bars derived during the data post-processing. Each figure is an RPM sweep at a constant wind tunnel test section velocity and model shaft angle in the tunnel. The sign convention for rotor shaft angle is as follows: -90 degrees shaft angle corresponds to axial climb, 0 degrees corresponds to edgewise flight, and +90 degrees corresponds to axial descent, as shown in Fig. 9.

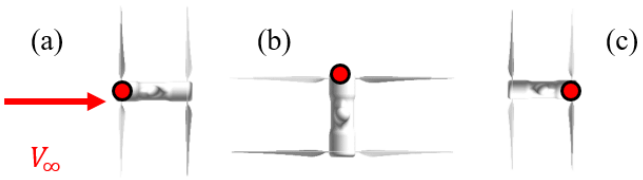

Figure 9. Shaft Angle Definition:
(a) Axial Climb (SA = -90 deg),
(b) Edgewise (SA = 0 deg),
(c) Axial Descent (SA = +90 deg).

HOVER CONDITIONS

Hover conditions for individual rotor performance of the coaxial rotor pair are reported in Figs. 10-11. The CFD data falls within the experimental data uncertainty bars for all points except the upper rotor at the highest rotor speed. The CFD appears to slightly over-predict thrust at high RPM. The individual rotor CFD torque predictions, however, are almost indistinguishable from the experimental data points.

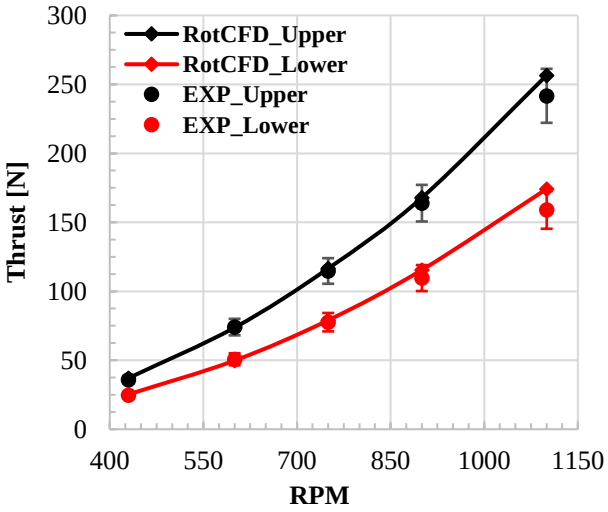

Figure 10. Hover - Thrust vs RPM.

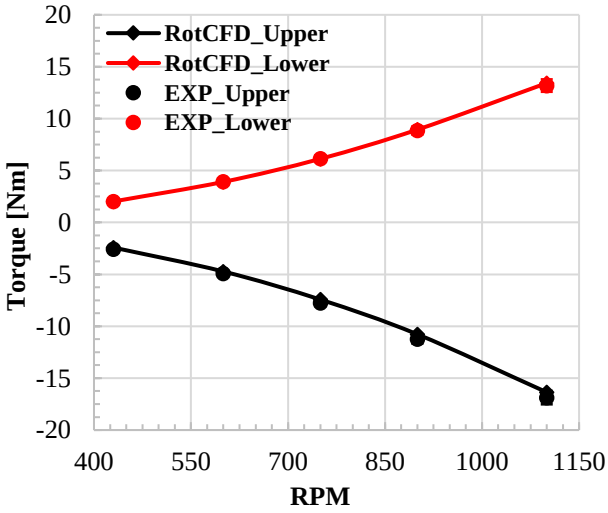

Figure 11. Hover - Torque vs RPM.

Figures 12-14 report the combined coaxial rotor performance comparisons for thrust, power, and figure of merit (FM), respectively. The CFD data points are again mostly within the experimental data uncertainty bars, except at the highest rotor speed, which is amplified and observed as a growing discrepancy in the FM at high rotor speed. Still, the comparisons are promising given the fidelity level and the high speed of the hybrid BEMT-URANS approach.

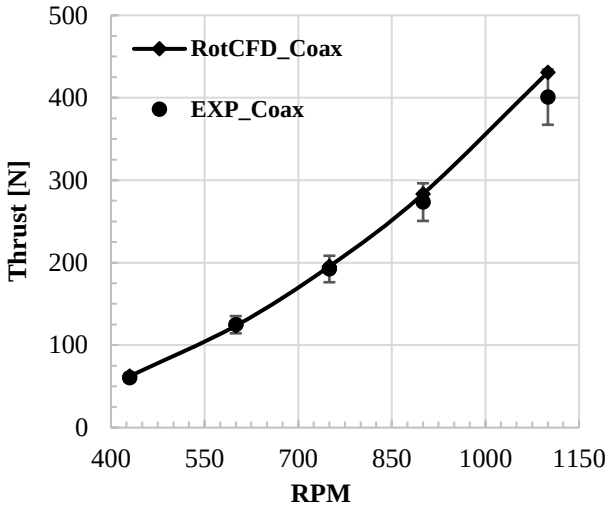

Figure 12. Hover - Coaxial Thrust vs RPM.

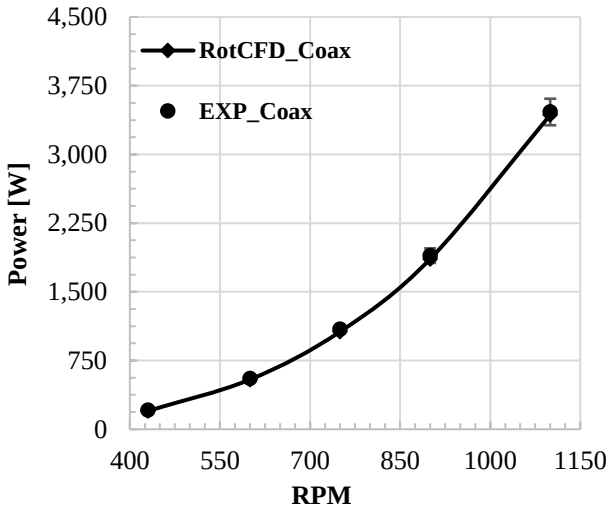

Figure 13. Hover - Coaxial Power vs RPM.

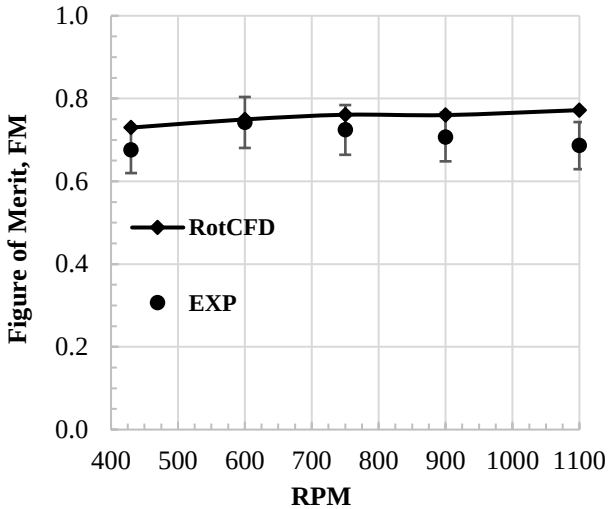

Figure 14. Hover - Coaxial FM vs RPM.

SLOW AXIAL CLIMB (TAKEOFF, SA=-90 DEG)

A slow-speed axial climb condition is reported in Figs. 15-17. This condition is relatively similar to hover, and the same general observations can be made as were done for the hover condition. One notable exception is that the CFD upper rotor thrust is no longer over-predicted. The lower rotor thrust, however, is still slightly over-predicted.

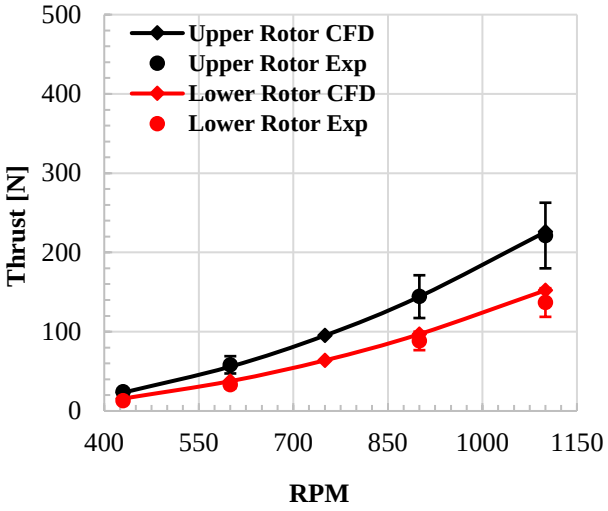

Figure 15. Slow Axial Climb - Thrust vs RPM. (SA = -90 deg, V = 2.25 m/s)

Rotor thrust comparisons are shown in Fig. 16. All the CFD predictions fall within the experimental uncertainty bars. The plot of torque vs. thrust in Fig. 17 further highlights any discrepancies between the CFD predictions and experimental measurements. All conditions again fall within the experimental uncertainty bars, indicating that the model works well for this slow axial climb condition, which could also be considered similar to an initial take-off condition.

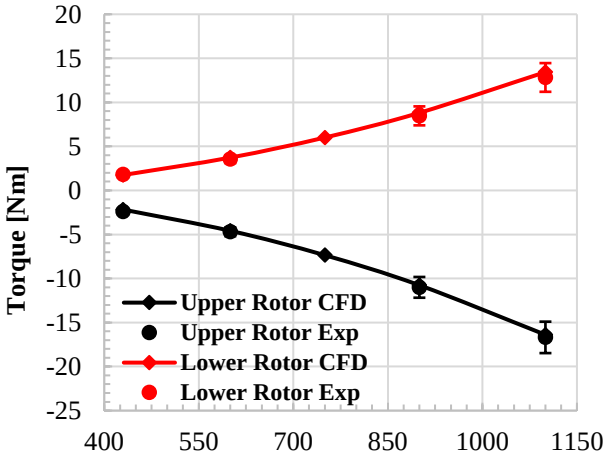

Figure 16. Slow Axial Climb - Torque vs RPM. (SA = -90 deg, V = 2.25 m/s)

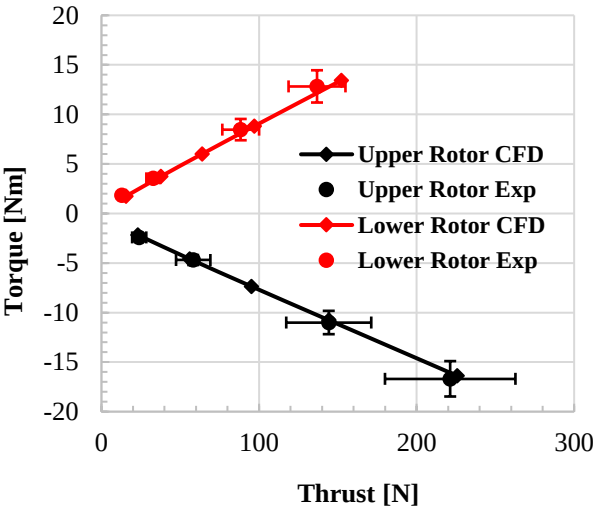

Figure 17. Slow Axial Climb - Torque vs Thrust. (SA = -90 deg, V = 2.25 m/s)

FORWARD FLIGHT (CRUISE, SA=-15 DEG)

Figures 18-20 report a forward-flight cruise-type condition. The shaft angle is 15 degrees nose-down with a wind tunnel test section velocity of 9 m/s. This flight condition could also be thought of as a shallow climb, but it would only be 'trimmed' steady-state flight for a single RPM. The CFD model predicts thrust within the experimental uncertainty bars for all conditions. For most RPMs, the predictions coincide with the experimental measurements. At high RPM, however, a slight discrepancy is observed with the upper rotor thrust being slightly overpredicted.

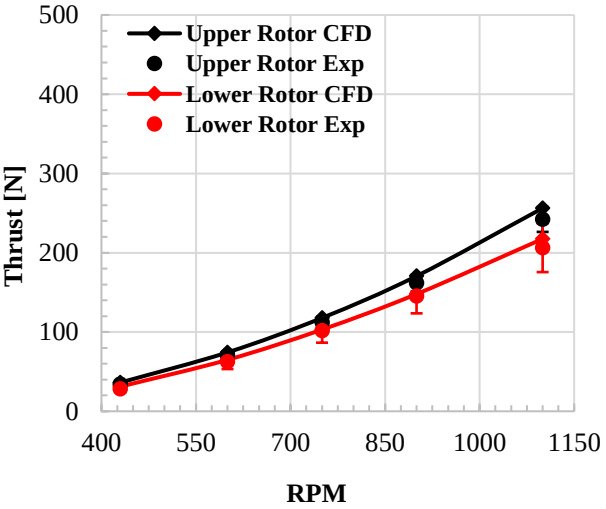

Figure 18. Forward Flight - Thrust vs RPM. (SA = -15 deg, V = 9 m/s)

The torque comparisons in Fig. 19 again show good agreement with all conditions appearing to be within the experimental uncertainty bars. Figure 20 highlights the upper rotor thrust over-prediction, but still shows values within the experimental uncertainty bars.

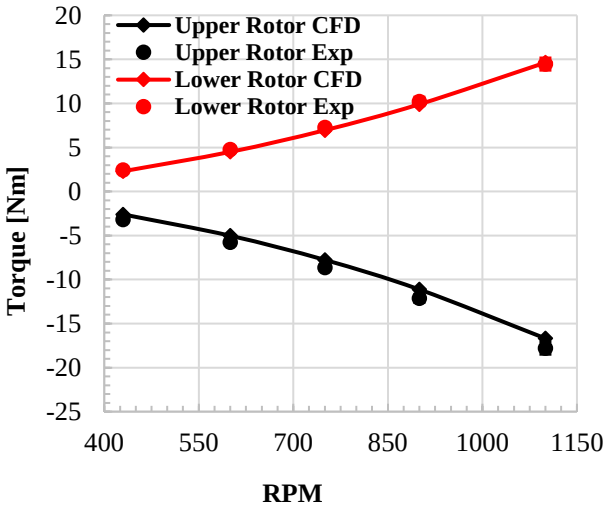

Figure 19. Forward Flight - Torque vs RPM. (SA = -15 deg, V = 9 m/s)

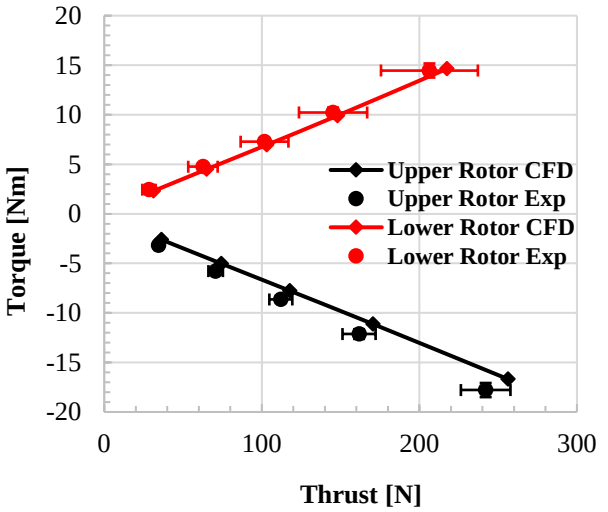

Figure 20. Forward Flight – Torque vs Thrust. (SA = -15 deg, V = 9 m/s)

FORWARD FLIGHT DESCENT (SA=+15 DEG)

The next portion of the flight envelope analyzed is forward flight descent, Figs. 21-23. This condition is at a moderate flight speed of six meters per second and has a rotor shaft angle of positive fifteen degrees. For UAM applications, this could be thought of as a glide-path approach to a runway or vertiport, as the vehicle comes in for landing. Figure 21 shows some interesting behavior with the lower rotor thrust predicted higher than the upper rotor thrust for a majority of the RPM sweep. This forward flight descent condition is challenging to predict due to the upwash at the front of the rotor disks and the downwash at the rear.

Figure 22 shows the torque predictions to be in good agreement, with the CFD data falling within the experimental uncertainty bars for almost all conditions. The lower rotor torque appears to be over-predicted at the highest RPM.

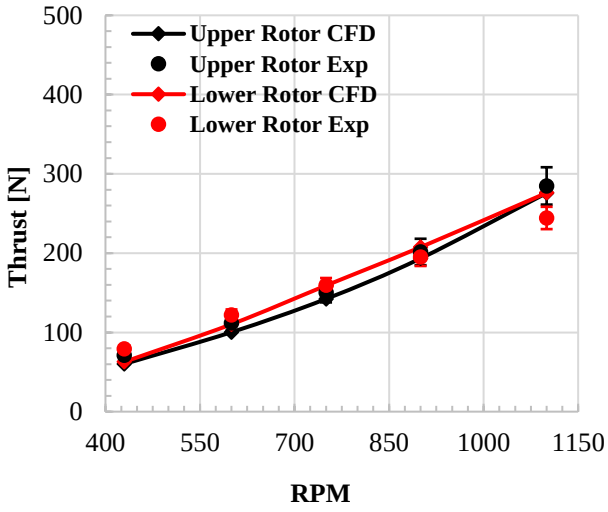

Figure 21. Forward Flight Descent - Thrust vs RPM. (SA = +15 deg, V = 6 m/s)

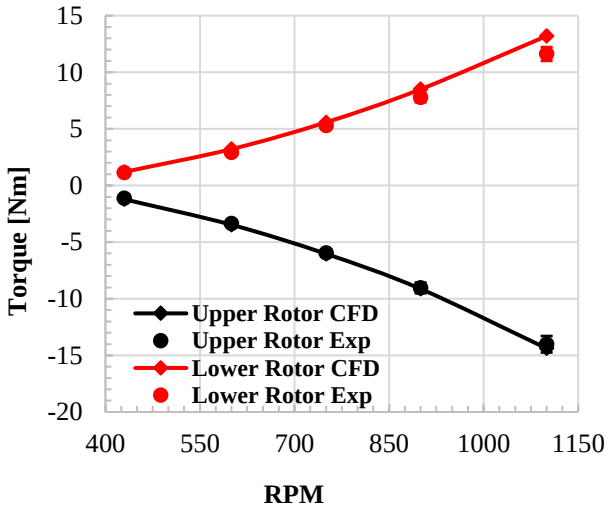

Figure 22. Forward Flight Descent - Torque vs RPM. (SA = +15 deg, V = 6 m/s)

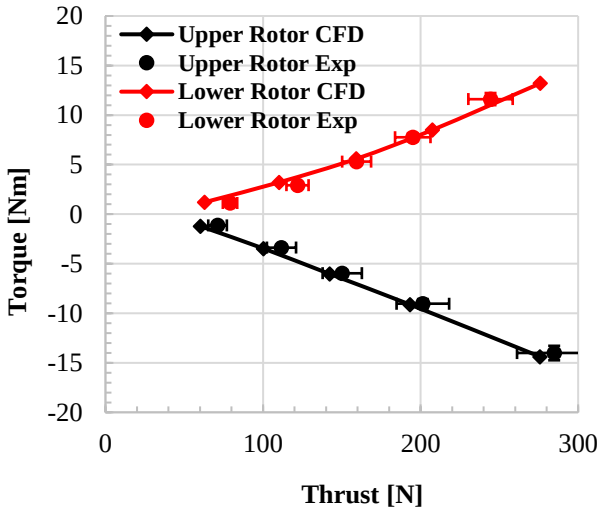

Figure 23. Forward Flight Descent - Torque vs Thrust. (SA = +15 deg, V = 6 m/s)

The last flight condition discussed in this brief validation study is axial descent. The first condition is a slow speed axial descent at 2.25 m/s. Figures 24-26 report the individual rotor comparisons for this condition. Even in axial descent, the CFD predictions are observed to generally fall within the experimental uncertainty bars with some limited exceptions. A close look at the low RPM range of Fig. 24 shows that the lower rotor thrust is actually higher than that of the upper rotor. This signifies some non-trivial rotor aerodynamics, and suggests that the lower rotor may already be experiencing some effects akin to the turbulent wake state. As the RPM is increased, the upper rotor thrust clearly increases above that of the lower rotor as expected. Throughout all conditions, torque is predicted within the experimental uncertainty bars.

AXIAL DESCENT (SA=+90 DEG)

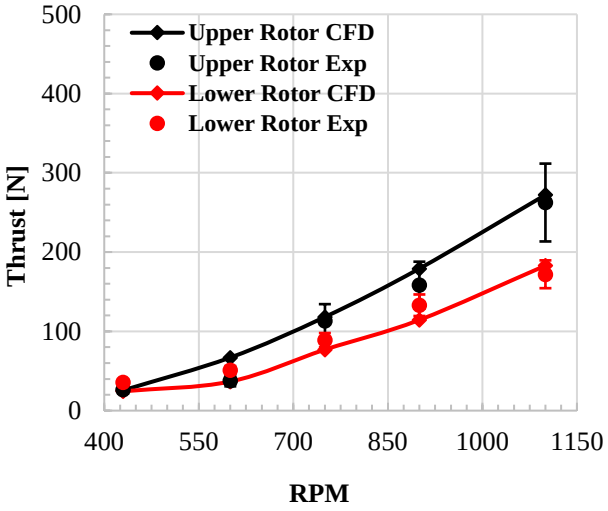

Figure 24. Slow Axial Descent - Thrust vs RPM. (SA = +90 deg, V = 2.25 m/s)

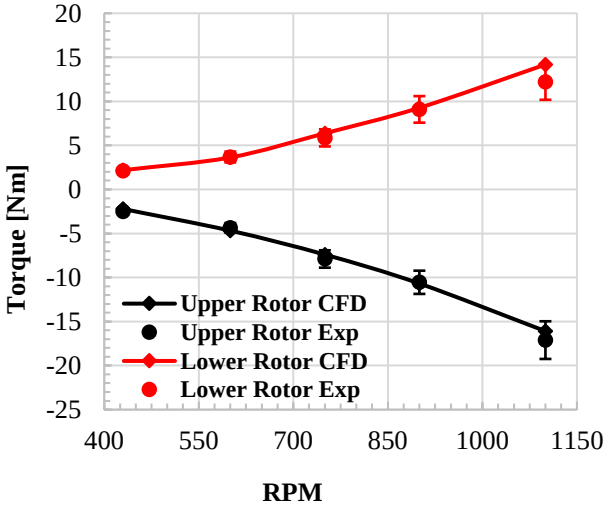

Figure 25. Slow Axial Descent - Torque vs RPM. (SA = +90 deg, V = 2.25 m/s)

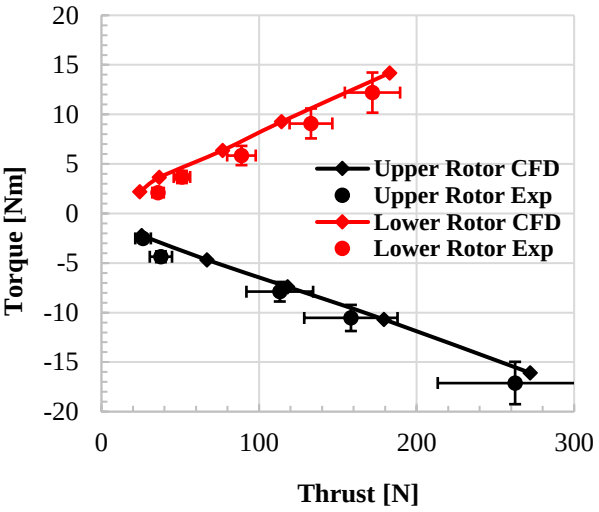

Figure 26. Slow Axial Descent - Torque vs Thrust. (SA = +90 deg, V = 2.25 m/s)

The next set of comparisons are once more axial descent, but this time at a higher rate of descent. Figures 27-29 report the comparisons at 4.5 m/s. At this higher descent rate, the lower rotor thrust in Fig. 27 is observed to be higher than the upper rotor thrust for about half of the RPM sweep. Figure 28 shows all torques remaining positive. Although not always within the experimental uncertainty bars, the rotor performance is typically close to the experimental measurements, which is impressive for the challenging nature of the condition. The highest RPM condition, however, indicates a large error between the predictions and experimental measurements. The uncertainty bars on thrust are also much higher for this condition. This indicates that this could be the Vortex Ring State (VRS), with large unsteady thrust fluctuations that are not captured by the time-averaged CFD prediction. The lower RPM conditions are likely to be in the Turbulent Wake State (TWS) and are approaching the windmill brake state (WBS) at the lowest RPM.

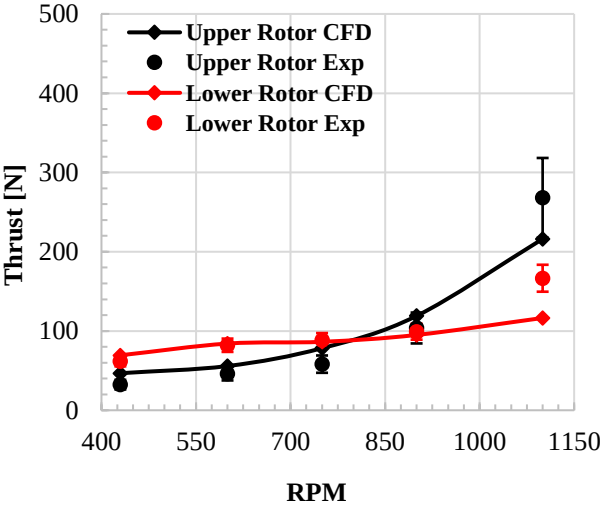

Figure 27. Moderate Axial Descent - Thrust vs RPM. (SA = +90 deg, V = 4.5 m/s)

The progression of rotor flow states in axial descent begins with the normal operating state, and progresses through VRS, then to TWS, and finally to WBS. When at a constant axial descent rate, such as the 4.5 m/s in Figs. 27-29, a very high RPM will most likely be in the normal operating state since $v_h \gg abs(V_z)$, such that $V_z/v_h > -0.5$. Then as you decrease RPM, i.e., moving left on the x-axes of Figs. 27-28, you are decreasing v_h at constant V_z. This increases the V_z/v_h ratio and pushes you to VRS, then to TWS, and finally to WBS as you decrease RPM on these plots moving from right to left. WBS can be observed when one of the rotor torques, typically the lower rotor, is approximately equal to zero.

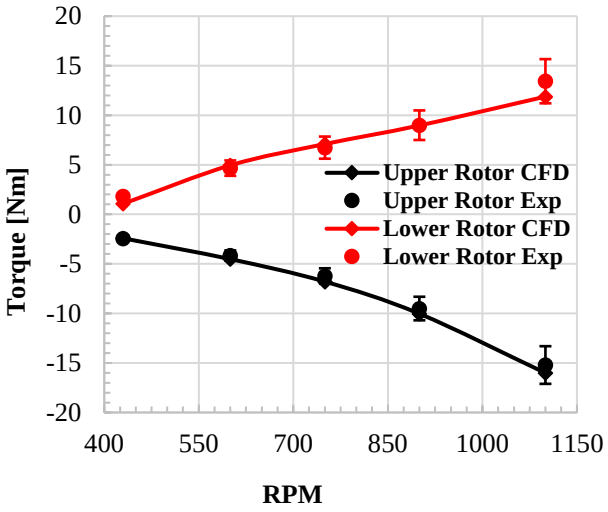

Figure 28. Moderate Axial Descent - Thrust vs RPM. (SA = +90 deg, V = 4.5 m/s)

Figure 29 shows a large discrepancy for the highest RPM condition. This could be indicative of large VRS unsteady thrust fluctuations, or possibly, a bad data measurement.

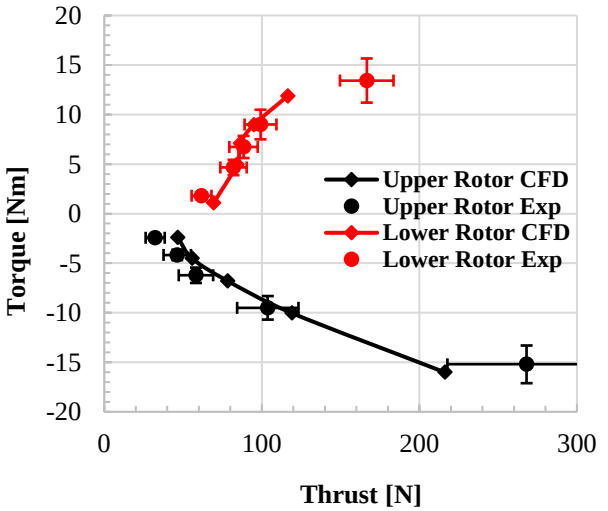

Figure 29. Moderate Axial Descent - Thrust vs RPM. (SA = +90 deg, V = 4.5 m/s)

The last set of comparisons are axial descent at the highest rate of descent. Figures 30-32 report the comparisons at 6 m/s. At this high descent rate, the lower rotor thrust in Fig. 30 is observed to be higher than the upper rotor thrust for most of the RPM sweep. Notably in Fig. 31, the first condition has a near-zero torque on the lower rotor, which indicates that condition as WBS. The CFD model appears to predict the emergence out of WBS a bit earlier than the experimental data show, as the lower rotor measured thrust is still higher than the upper rotor measured thrust even at the maximum RPM condition.

The torque vs. thrust comparisons in Fig. 32 have a bit higher discrepancy than previously observed. Considering the challenging condition being simulated, however, the comparisons are close to being within the experimental uncertainty bounds. The first points at 430 RPM show a near-zero torque for the lower rotor, indicating WBS. As the rotor speed increases, a driving torque is quickly required on the lower rotor indicating its exit from WBS towards TWS.

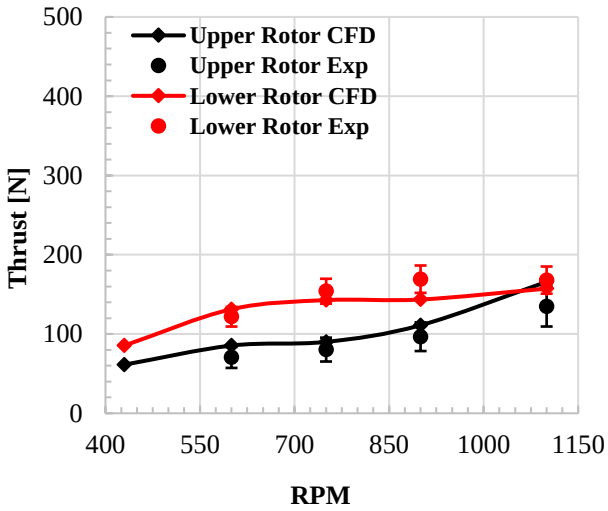

Figure 30. Fast Axial Descent - Thrust vs RPM. (SA = +90 deg, V = 6 m/s)

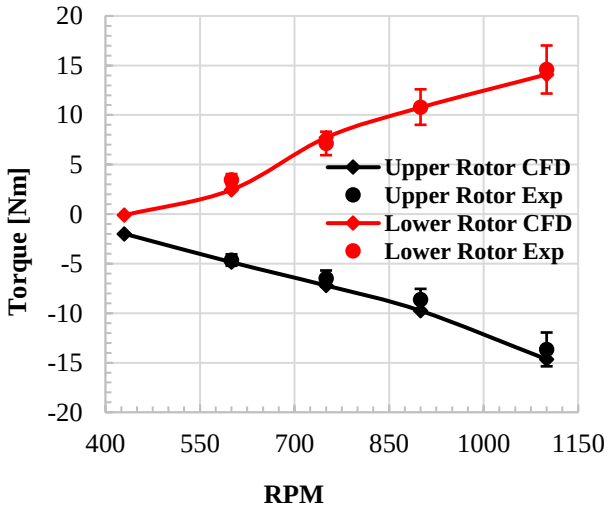

Figure 31. Fast Axial Descent - Torque vs RPM. (SA = +90 deg, V = 6 m/s)

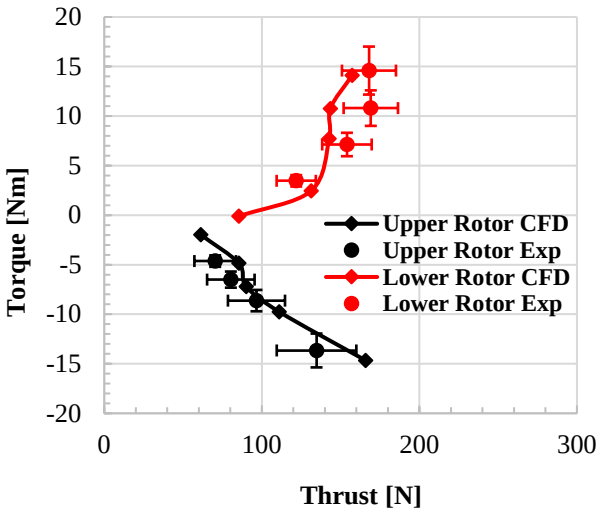

Figure 32. Fast Axial Descent – Torque vs Thrust. (SA = +90 deg, V = 6 m/s)

Overall, the data are in good agreement. Comparisons at low wind tunnel speed, i.e. close to hover conditions, are almost exactly aligned. Although the data are generally in very good agreement, larger discrepancies can be observed at high flight speeds and in challenging rotor aerodynamic flow states such as VRS. This is due to higher rotor-rotor interaction in conditions such as climb and a higher distortion of the azimuthal inflow distribution in other conditions such as high advance ratio forward flight. Further information for this coaxial rotor system and related modeling predictions in VRS can be found in Ref. [52]. Comparison metrics are reported in Table 1 in percentages, dimensional units, and root-mean-squared error.

Table 1. Summary of Average CFD vs. TDT Data Comparisons.

	Upper Thrust [N]	Upper Torque [Nm]	Lower Thrust [N]	Lower Torque [Nm]
Average	7.24%	-0.88%	0.45%	4.52%
Average	6.31 N	0.02 Nm	-1.32 N	0.28 Nm
RMSE	17.58 N	0.80 Nm	18.32 N	0.83 Nm

MACHINE LEARNING

Many concepts and approaches of machine learning (ML) have been around for some time, with the term itself dating back to 1959, but their adoption for aerospace applications has been slower than for computer science and other data-driven fields. Figure 33 shows the relationship between several common approaches that fall under the very broad ML umbrella. This work uses MATLAB's Regression Learner toolbox to create and test rotor performance surrogate models using various methods of supervised machine learning. A more thorough review of machine learning applications in aerospace, including surrogate modeling and data upscaling, can be found in Ref. [9].

ML METHODOLOGY

The MATLAB Regression Learner toolbox includes many common supervised machine learning methods including linear regression, support vector machines, regression trees, ensemble of trees, Gaussian process regression (GPR), and

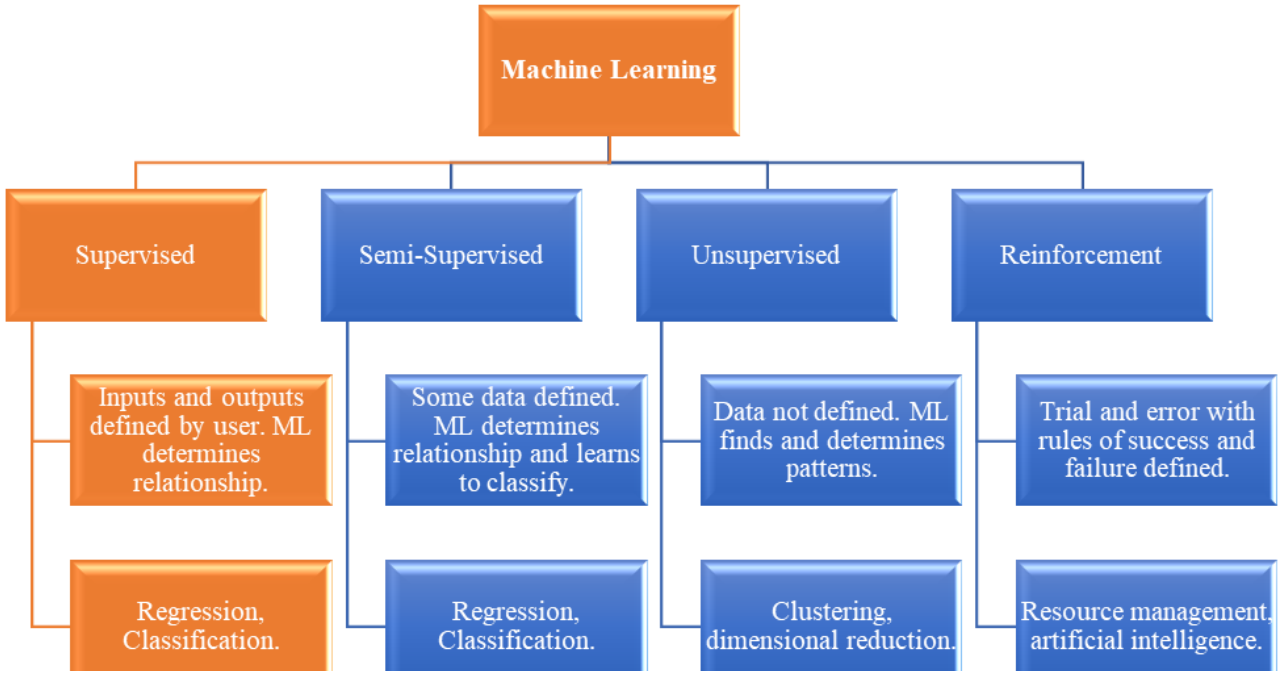

Figure 33. Summary of Machine Learning Approaches and Some Common Applications.

neural networks. As identified in this and previous work, GPR is generally a good model for interpolation of these rotor performance tables. Gaussian process regression was found in this study to consistently give the lowest root-mean-squared-error (RMSE) metrics with either a rational quadratic or Matérn kernel. This is likely because the rotor performance, thrust as an example, scales with RPM squared. In addition to that relationship, the GPR model is reliable at modeling highly non-linear high-dimensionality data. All models included in the MATLAB toolbox were tested.

ML SURROGATE MODEL TRAINING

For this section on machine learning surrogate modeling, the CFD datasets were used as training data. A few major distinctions are used to discretize the training datasets. The first major distinction is the rotor configuration, which is either coaxial or single rotor. The coaxial rotor dataset corresponds to the setup depicted in Figs. 5, 7, and 8. The single rotor dataset uses an identical CFD model, with the exception that one of either the upper or lower rotors has been removed.

The test conditions for the coaxial rotor dataset are reported in Fig. 34. This chart displays the test conditions on a rotor aerodynamic state chart. The x-axis is a non-dimensionalized horizontal speed parameter, and the y-axis is a non-dimensionalized vertical speed parameter. This allows for the reduction of the three-dimensional input space (i.e. shaft angle, velocity, and RPM) into a two-dimensional reduced latent-space. Of special note is that the chart can still be discretized by rotor shaft angle, where the negative y-axis is axial descent and the positive y-axis is axial climb. The shaft angle increases in a counter-clockwise fashion around the origin. A red line depicts the empirical VRS boundary, Ref. [64].

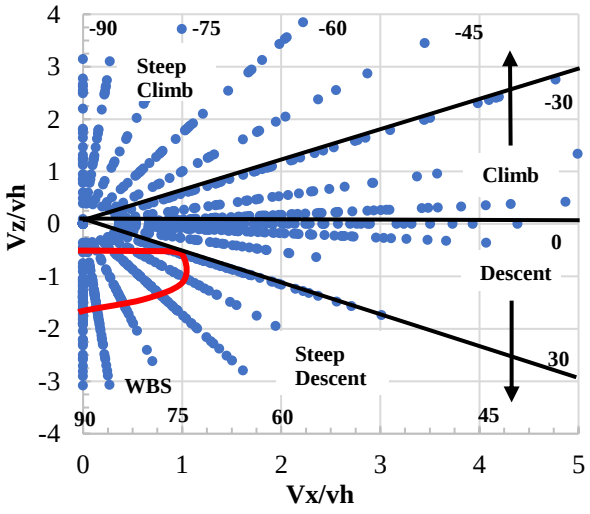

Figure 34. Coaxial Rotor CFD Dataset – 930 Conditions Rotor Aerodynamic State Chart.

The figure shows the very wide range of flight conditions included in the CFD training dataset, which goes far beyond what would likely be considered typical operation for a UAM vehicle. Additionally, many conditions were simulated in adverse rotor aerodynamic flow states such as VRS, WBS and TWS. The dataset is composed of coaxial rotor performance data using both atmospheres tested in the NASA Langley Transonic Dynamics Tunnel: R134-a heavy gas and air. Roughly 63% of the simulations are using the heavy gas aerodynamic properties, while 37% are using air.

Figure 35 shows the same coaxial rotor simulations, but with the axes changed to advance ratio and inflow ratio. The VRS boundary has been removed in this plot since the two parameters are not nondimensionalized by v_h. This gives an idea of the typical rotor conditions being simulated. Some very high advance ratios are achieved with the combination of a high free-stream velocity and low rotor RPM, but the majority of simulations have advance ratio less than 0.25. The cruise condition shown in the CFD model validation section, Figs. 18-20, has advance ratios of approximately 0.15 to 0.20 for RPMs of 900 and 750, respectively.

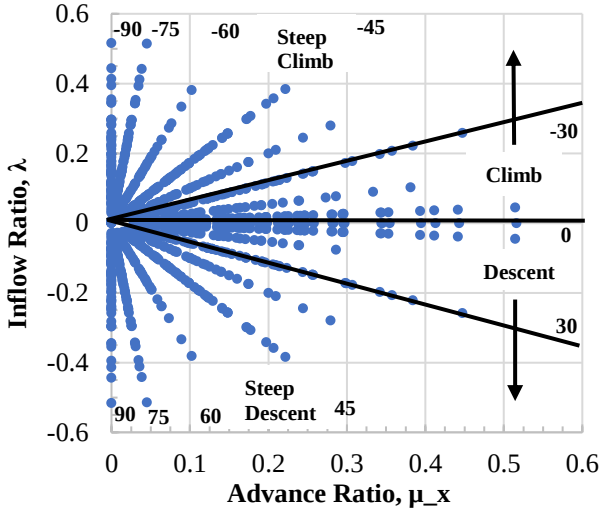

Figure 35. Coaxial Rotor CFD Dataset – 930 Conditions Inflow Ratio vs Advance Ratio.

Figure 36 depicts the single rotor CFD training dataset. This dataset again includes simulations using both the R134-a heavy gas and air atmospheric conditions. Although the same bounds of the non-dimensional rotor aerodynamic state chart are covered, the dataset is much sparser than the coaxial rotor dataset. Notably, it excludes a few of the rotor shaft angles that are included in the coaxial rotor datasets.

The single rotor dataset does, however, cover a similar range of the rotor aerodynamic state chart. This is because the bounds of the wind tunnel test for both the single and coaxial rotor configurations were approximately the same. The emphasis in this work is on the coaxial rotor dataset, but past work has quantified the RotCFD tool's single rotor prediction capability, Ref. [51].

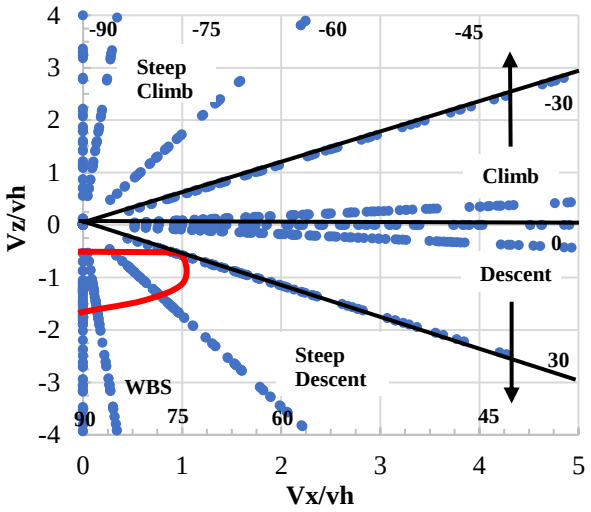

Figure 36. Single Rotor CFD Dataset – 520 Conditions.

Results are first shown for the coaxial rotor dataset. Surrogate models were trained with the previously mentioned supervised training methods. In almost all cases, GPR was found to provide the lowest model RMSE. The RMSE and other test statistics for the surrogate models were calculated using a 5-fold cross validation strategy, which is commonly employed for small datasets. The k-fold cross validation provides metrics on model accuracy while simultaneously preventing against over-fitting the data. Although these datasets represent nearly 2,000 distinct CFD simulations, it is still a relatively small number for machine learning applications. The small size of the dataset means all models tested can be trained and analyzed in reasonable amounts of time. With much larger datasets, however, GPR would become computationally expensive and neural networks potentially more appealing.

The models were trained using various combinations of input parameters including rotor shaft angle, flight speed, RPM, advance ratio, inflow ratio, and density. The best models used all input parameters, although density was only used for the combined dataset that had simulations in both air and heavy gas. Model RMSE values for coaxial rotor thrust and power prediction are reported in Table 2 for the combined dataset, the R134-a heavy gas dataset, and the air dataset.

Table 2. ML Coaxial Rotor Surrogate Model Performance (best model for each dataset).

Dataset	Coaxial Rotor Thrust RMSE	Coaxial Rotor Power RMSE
Coaxial: All	4.4%	8.5%
Coaxial: R134-a	4.2%	6.8%
Coaxial: Air	4.5%	11.1%

Interestingly, the combined surrogate model with density included as a parameter did quite well at predicting the dimensional rotor thrust and power. This suggests that a surrogate model could be used to reliably predict, or maybe adjust, multirotor performance under various atmospheric conditions.

The single rotor dataset was only trained as a single combined dataset. The atmospheric density, rotor shaft angle, flight speed, RPM, advance ratio, and inflow ratio were again used as input parameters. The RMSE values for the best model's prediction of rotor thrust and power are reported in Table 3. The table compares the RMSE values for two different models, one using all six of the input parameters and another that leaves out the advance ratio and inflow ratio. Interestingly, the model with less input parameters has slightly lower RMSE values for both thrust and power prediction. This is contrary to what was observed in the model generation for the coaxial rotor database, where all models were more accurate when including all six of the input parameters in the model.

Table 3. ML Single Rotor Surrogate Model Performance (using two different sets of input variables).

Dataset: Single Rotor, Air and Heavy Gas	Single Rotor Thrust RMSE	Single Rotor Power RMSE
Density, SA, V, RPM, Mu_x, Mu_z	6.3%	10.4%
Density, SA, V, RPM	5.8%	10.3%

Figure 37 highlights the data upscaling capability of these surrogate models and their speed towards real-time simulation, rapid design optimization, and Monte Carlo Simulation. Using the best R134-a heavy gas surrogate model, the coaxial rotor thrust was predicted for 3 million flight conditions within the bounds of the training data. This was calculated in MATLAB on a single CPU core in 19.63 seconds, or about 6 millionths of a second per flight condition. By extension, coaxial rotor thrust and power can be predicted in approximately 12 millionths of a second per flight condition, and individual rotor thrust and power within 24 millionths of a second per condition.

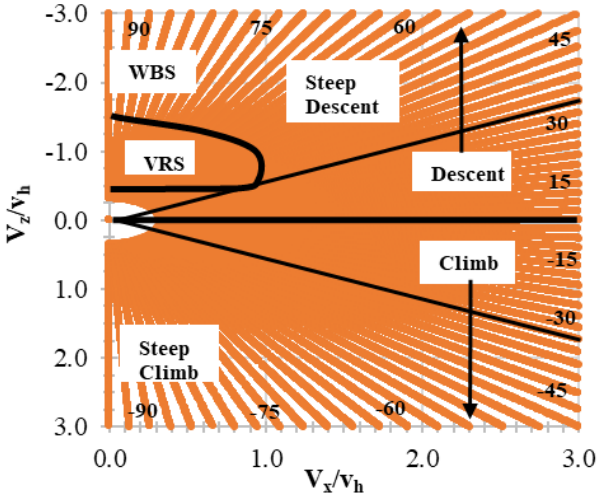

Figure 37. Upscaling the Coaxial Rotor Dataset using Surrogate Models (6e-6 s per Flight Condition).

IMPLICATIONS OF THIS WORK ON UAM DESIGN TRADE STUDIES

As mentioned in this paper's introduction, past work has investigated multirotor configurations for the NASA UAM reference design missions, Ref. [5, 10-13]. A recent design study of a coaxial quadrotor for UAM, with a similar configuration as discussed in this work, showed promise for the coaxial rotor system's applicability, Ref. [65]. This UAM coaxial quadrotor reference design study was an excursion expanding upon a multiyear study in quadrotor configurations for UAM reference missions. Figure 38 depicts an example of the coaxial quadrotor UAM reference vehicle.

Figure 38. "Designing a Coaxial Quadrotor for Urban Air Mobility," Reproduced from Ref. [65].

There are significant differences between the above coaxial quadrotor design and recent coaxial rotor systems tested in the NASA LaRC 14- by 22- ft. Subsonic Tunnel Facility, Ref. [51], and the LaRC TDT (this work). There are, however, many similarities both configuration-wise and with the underlying aerodynamics and aeromechanics challenges between these rotor systems. A subset of the coaxial quadrotor designs being proposed leverage the fixed-pitch variable-speed rotor design, which is the type of configuration this work analyzed.

In particular, the machine learning approach outlined in this paper has promise to transform the methodology to perform conceptual and preliminary design for multirotor aircraft. The surrogate models, for example, can be used to increase the accuracy of aircraft parametric design and aircraft design optimization. Furthermore, once a preliminary design has been reached, the surrogate modeling can be used to make highly efficient models towards performance analysis and real-time flight simulation. Prediction speed on the order of six millionths of a second per flight condition were demonstrated in this work, with accuracy of order 5-10% to the underlying CFD.

CONCLUSIONS

This work presents validation of an improved CFD methodology for performance analysis of fixed-pitch variable-speed multirotor aircraft, especially those using coaxial rotor pairs operating over a wide range of flight conditions. A brief background on the use of this rotor configuration in UAM, eVTOL, and planetary exploration was presented. A recent coaxial rotor test campaign conducted in the NASA Langley Research Center's Transonic Dynamics Tunnel (TDT) was briefly discussed and was used as validation data in this work. The rotor system tested was a fixed-pitch variable-speed coaxial rotor relevant to the previously mentioned applications.

The creation of a hybrid BEMT-URANS CFD model was briefly described, along with novel approaches for the generation of the C81 airfoil performance look-up tables using the OVERFLOW CFD solver. These steps improve the accuracy of rotor-modeled computational approaches using BEMT, and the accuracy was demonstrated here in the context of the hybrid BEMT-URANS CFD flow solver, RotCFD. Individual rotor thrust and torque for the coaxial rotor system was predicted within an average of 5-10% of the experimental data, which spanned nearly 600 wind tunnel test conditions for the coaxial rotor operating in R134-a heavy gas.

Additionally, various methods in supervised machine learning were tested to develop rotor performance surrogate models using both the coaxial and single rotor CFD training datasets. These datasets consisted of nearly 2,000 discrete coaxial rotor CFD simulations run on the NASA Pleaides supercomputer. Gaussian process regression was consistently found to generate surrogate models with the lowest root-mean-squared error (RMSE) for the various datasets. The best model, identified here by lowest RMSE, had RMSE for coaxial thrust and torque of 4.4% and 8.5%, respectively.

Model inputs of rotor shaft angle, flight speed, RPM, advance ratio, inflow ratio, and density were used. For the coaxial rotor dataset, using all the input parameters resulted in the most accurate models. The single rotor dataset, however, had better models when omitting the advance ratio and inflow ratio, which is likely due to the large discrepancy between the dimensional and non-dimensional parameters.

The final coaxial rotor surrogate model was used to generate a three million flight condition look-up table in 19.6 seconds on a single CPU core using MATLAB. This equates to roughly 6 millionths of a second per prediction, or roughly 12 millionths of a second for coaxial rotor thrust and power. This highlights the potential for transformational approaches by combining mid-to-high fidelity simulation data with machine learning towards surrogate model generation. The resulting surrogate models can improve the aerodynamic modeling accuracy with minimal computational cost for applications such as design optimization, real-time flight simulation, and Monte Carlo Simulation. This surrogate modeling methodology could provide major advancements in the aerodynamic design, analysis, and simulation of terrestrial eVTOL and UAM aircraft, as well as planetary aerial vehicles supporting future space exploration missions.

Author contact: Dr. Jason Cornelius
jason.k.cornelius@nasa.gov

ACKNOWLEDGMENTS

This work was funded by the NASA New Frontiers Dragonfly Mission. The authors would like to thank the NASA Langley Transonic Dynamics Tunnel staff and the Dragonfly experimental test team for obtaining and post-processing the experimental data. The authors also thank the NASA Advanced Supercomputing Division for their support in using the High-End Computing Capability Pleaides GPU nodes for this work.

Lastly, the authors express their sincerest gratitude to Nappinai Rajagopalan and the late Dr. Ganesh Rajagopalan for the development and continued support of the RotCFD and AFTGen tools that have been instrumental in conducting engineering design and analysis in support of many planetary exploration studies and missions discussed in this work.

REFERENCES

1. Young, L.A., et al, "New Concepts and Perspectives on Micro-Rotorcraft and Small Autonomous Rotary-Wing Vehicles," 20th AIAA Applied Aerodynamics Conference, St. Louis, MO, June 24-27, 2002.
2. Young, L.A., "Aerobots as a Ubiquitous Part of Society," AHS Vertical Lift Aircraft Design Conference, San Francisco, CA, January 18-20, 2006.
3. Young, L.A., "Future Roles for Autonomous Vertical Lift in Disaster Relief and Emergency Response," Heli-Japan 2006: AHS International Meeting on Advanced Rotorcraft Technology and Life Saving Activities, Nagoya, Japan, November 15-17, 2006.
4. Young, L.A., "Conceptual Design Aspects of Three General Sub-Classes of Multi-Rotor Configurations: Distributed, Modular, and Heterogeneous," Sixth AHS International Specialists Meeting on Unmanned Rotorcraft Systems, Scottsdale, AZ, January 20-22, 2015.
5. Johnson W. and Silva C., "NASA concept vehicles and the engineering of advanced air mobility aircraft," *The Aeronautical Journal*, pp. 1-33, 2021. https://doi.org/10.1017/aer.2021.92
6. Alonso, J.J., Arneson, H.M., Melton, J.E., Vegh, J.M., Walker, C., and Young, L.A., "System-of-Systems Considerations in the Notional Development of a Metropolitan Aerial Transportation System: Implications as to the Identification of Enabling Technologies and Reference Designs for Extreme Short Haul VTOL Vehicles with Electric Propulsion," NASA TM 2017-218356, September 2017 .
7. The Vertical Flight Society, "eVTOL Aircraft Directory," Accessed 1/11/2024. https://evtol.news/aircraft.
8. Newton, L., "Second Chance to Join NASA's National Campaign Opens," NASA Armstrong, Feb. 2021. https://www.nasa.gov/centers/armstrong/features/second-chance-to-join-NASAs-national-campaign-opens.html
9. Cornelius, J., "Mid-Fidelity Performance Analysis for Fixed-Pitch Speed-Controlled Multirotor Aircraft," Doctoral Dissertation, The Pennsylvania State University, August 2023.
10. Silva, C., Johnson, W., Solis, E., "Concept Vehicles for VTOL Air Taxi Operations," AHS Technical Meeting on Aeromechanics Design for Vertical Lift, Holiday Inn at Fisherman's Wharf, San Francisco, CA, Jan. 16-18, 2018. https://rotorcraft.arc.nasa.gov/Publications/files/Johnson_2018_TechMx.pdf
11. Silva, C., Johnson, W., Antcliff, K. R., and Patterson, M.D., "VTOL Urban Air Mobility Concept Vehicles for Technology Development," 2018 Aviation Technology, Integration, and Operations Conference, AIAA Aviation Forum, AIAA 2018-3847, Dallas, TX, June 2018. https://doi.org/10.2514/6.2018-3847
12. Antcliff, K., Whiteside, S., Kohlman, L., and Silva, C., "Baseline Assumptions and Future Research Areas for UrbanAir Mobility Vehicles," AIAA SciTech, AIAA-2019-0528, May 28, 2019. https://doi.org/10.2514/6.2019-0528
13. Silva, C., Johnson, W., "Practical Conceptual Design of Quieter Urban VTOL Aircraft," Presented at the Vertical Flight Society's 77th Annual Forum & Technology Display, Virtual, May 10–14, 2021. https://rotorcraft.arc.nasa.gov/Publications/files/77-2021-0202_Silva.pdf
14. Russell, C., Willink, G., Theodore, C., Jung, J., and Glasner, B., "Wind Tunnel and Hover Performance Test Results for Multirotor UAS Vehicles," NASA/TM02018-219758, Feb. 2018. https://rotorcraft.arc.nasa.gov/Publications/files/Russell_1180_Final_TM_022218.pdf
15. Gregory, D., Cornelius, J.,Waltermire, S., Loob, C., and Schatzman, N., "Acoustic Testing of Five Multirotor UAS in the U.S. Army 7- by 10-Foot Wind Tunnel," NASA/TM-2018-219894, May 2018. https://rotorcraft.arc.nasa.gov/Publications/files/Schatzman_TM_2018_219894_Final.pdf
16. Schatzman, N., "Aerodynamics and Aeroacoustic Sources of a Coaxial Rotor," NASA/TM-2018-219895, Nov. 2018. https://rotorcraft.arc.nasa.gov/Publications/files/Schatzman_TM_2018_219895_Final.pdf
17. Yoon, S., Lee, H., and Pulliam, T., "Computational Analysis of Multirotor Flows," AIAA 2016-0812, Jan. 2016. https://doi.org/10.2514/6.2016-0812
18. Yoon, S., Lee, H., and Pulliam, T., "Computational Study of Flow Interactions in Coaxial Rotors," AHS Technical Meeting on Aeromechanics Design for Vertical Lift, Jan. 2016. https://ntrs.nasa.gov/archive/nasa/casi.ntrs.nasa.gov/20160001149.pdf
19. Yoon, S., Chan, W., and Pulliam, T., "Computations of Torque-Balanced Coaxial Rotor Flows," AIAA 2017-0052, Jan. 2017. https://doi.org/10.2514/6.2017-0052

20. Yoon, S., Diaz, P., Boyd, D., Chan, W., and Theodore, C., "Computational Aerodynamic Modeling of Small Quadcopter Vehicles," AHS 73rd Annual Forum, May 2017. https://rotorcraft.arc.nasa.gov/Publications/files/73_2017_0015.pdf
21. Grip, H., Johnson, W., Malpica, C., Scharf, D., Mandic, M., Young, L., Allan, B., Mettler, B., Martin, M., Lam, J., "Modeling and Identification of Hover Flight Dynamics for NASA's Mars Helicopter," *AIAA Journal of Guidance, Control, and Dynamics*, Vol. 43, No.2, Feb. 2020. https://doi.org/10.2514/1.G004228
22. Balaram, J., Canham, T., Duncan, C., Golombek, M., Grip, H., Johnson, W., Maki, J., Quon, A., Stern, R., Zhu, D., "Mars Helicopter Technology Demonstrator," AIAA SciTech Forum, AIAA-2018-0023, Kissimmee, Florida, 2018. https://doi.org/10.2514/6.2018-0023
23. Koning, W., Johnson, W., and Grip, H., "Improved Mars Helicopter Aerodynamic Rotor Model for Comprehensive Analyses," *AIAA Journal*, Vol. 57, No. 9, Sept. 2019. https://doi.org/10.2514/1.J058045
24. Koning, W., "Generation of Performance Model for the Aeolian Wind Tunnel (AWT) Rotor at Reduced Pressure," NASA/CR–2018–219737, Dec. 2018. https://ntrs.nasa.gov/citations/20180008699
25. Dull, C., Wagner, L., Johnson, W, Young, L.A., "Hover and Forward Flight Performance Modeling of Ingenuity," Vertical Flight Society Transformative Vertical Flight Conference, San Jose, CA January 25-27, 2022.
26. Lorenz, R. D., Turtle, E. P., Barnes, J. W., Trainer, M. G., Adams, D. S., Hibbard, K. E., Sheldon, C. Z., Zacny, K., Peplowski, P. N., Lawrence, D. J., Ravine, M. A., McGee, T. G., Sotzen, K. S., MacKenzie, S. M., Langelaan, J. W., Schmitz, S., Wolfarth, L. S., and P. D. Bedini, "Dragonfly: a rotorcraft lander concept for scientific exploration at Titan," Johns Hopkins APL Technical Digest Vol. 34, No. 3, pp. 374-387, 2018. https://dragonfly.jhuapl.edu/News-and-Resources/docs/34_03-Lorenz.pdf
27. Cornelius, J., Opazo, T., Schmitz, S., Langelaan, J., Villac, B., Adams, D., Rodovskiy, L., Young, L., "Dragonfly – Aerodynamics during Transition to Powered Flight," VFS 77th Annual Forum, May, 2021. https://rotorcraft.arc.nasa.gov/Publications/files/77-2021-0264_Cornelius.pdf
28. Langelaan, J., Schmitz, S., Palacios, J., Lorenz, R., "Energetics of rotary-wing exploration of Titan," IEEE Aerospace Conference, 2704, 2017. https://doi.org/10.1109/AERO.2017.7943650
29. Lorenz, R., Schmitz, S., Kinzel, M., "Prediction of aerodynamically-triggered condensation: Application to the Dragonfly rotorcraft in Titan's atmosphere," Aerospace Science and Technology, 114, 106738, 2021. https://doi.org/10.1016/j.ast.2021.106738
30. Langelaan, J., Schmitz, S., Adams, D., Lorenz, R., "Conceptual Design of the Dragonfly Lander," Vertical Flight Society Annual Forum 77, 2021.
31. J.W. Barnes, E.P. Turtle, M.G. Trainer, R.D. Lorenz, S.M. MacKenzie, W.B. Brinckerhoff, M.L. Cable, C.M. Ernst, C. Freissinet, K.P. Hand, A.G. Hayes, S.M. Hurst, J.R. Johnson, E. Karkoschka, D.J. Lawrence, A. Le Gall, J.M. Lora, C.P. McKay, R.S., "Science Goals and Objectives for the Dragonfly Titan Rotorcraft Relocatable Lander," *The Planetary Science Journal*, Vol. 2, No. 18, 2021. https://doi.org/10.3847/PSJ/abfdcf
32. Greicius, T., "6 Things to Know About NASA's Ingenuity Mars Helicopter," NASA/JPL-CalTech, Pasadena, CA, Apr. 2021. https://www.nasa.gov/feature/jpl/6-things-to-know-about-nasas-ingenuity-mars-helicopter
33. Talbert, T., Gribben, S., "NASA's Dragonfly Team Soars through Major Design Review," NASA/Johns Hopkins APL, Mar. 2023. https://www.nasa.gov/feature/nasa-s-dragonfly-team-soars-through-major-design-review
34. Young, L. A., Chen, R. T. N., Aiken, E. W., Briggs, G. A., "Design Opportunities and Challenges in the Development of Vertical Lift Planetary Aerial Vehicles," Proceedings of the American Helicopter Society International Vertical Lift Aircraft Design Specialist's Meeting, January 2000.
35. Young, L. A., "Vertical Lift - Not Just for Terrestrial Flight," Proceedings of the AHS/AIAA/RaeS/SAE International Powered Lift Conference, Arlington, VA, October 30- November 1, 2000.
36. Young, L. A., "Exploration of Titan Using Vertical Lift Aerial Vehicles," Forum on Innovative Approaches to Outer Planetary Exploration 2001–2020, Feb. 2001.
37. Young, L. A., and Aiken, E. W., "Vertical Lift Planetary Aerial Vehicles: Three Planetary Bodies and Four Conceptual Design Cases," Presented at 27th European Rotorcraft Forum, Moscow, Russia, September 11-14, 2001.
38. Young, L.A., "Exploration of Titan Using Vertical Lift Aerial Vehicles," NASA Headquarters and Lunar and Planetary Institute Forum on Innovative Approaches to Outer Planetary Exploration, LPI Contribution # 1084, Houston, TX, February 21-22, 2001.
39. Young, L. A., Aiken, E. W., Derby, M. R., Johnson, J. L., Navarrete, J., Klem, J., Demblewski, R., Andrews, J. and Torres, R. "Engineering Studies into Vertical Lift Planetary Aerial Vehicles," Presented at the AHS International Meeting on Advanced Rotorcraft Technology and Life Saving Activities, Tochigi, Japan, November 2002.
40. Young, L.A., Pisanich, G., and Ippolito, C., "Aerial Explorers," 43rd AIAA Aerospace Sciences Meeting, Reno, NV, January 10-13, 2005.
41. Young, L., Pascal, L., Aiken, E., Briggs, G., Withrow–Maser, S., Pisanich, G., Cummings, H., "The Future of Rotorcraft and other Aerial Vehicles for Mars Exploration," Presented at the Vertical Flight Society's 77th Annual Forum & Technology Display, Virtual, May 10-14, 2021. https://rotorcraft.arc.nasa.gov/Publications/files/77-2021-0064_Young.pdf

42. Radotich, M., Withrow–Maser, S., deSouza, Z., Gelhar,S., Gallagher H., "A Study of Past, Present, and Future Mars Rotorcraft," Presented at the Vertical Flight Society's 9th Biennial Autonomous VTOL Technical Meeting, Virtual, January 26-28, 2021. https://rotorcraft.arc.nasa.gov/Publications/files/Radotich_aVTOL_Tech_Meeting_Final_Revised_012521.pdf
43. Young, L., Deluane J., Johnson W., Withrow–Maser, S., Cummings, H., Sklyanskiy E., Izraelevitz J., Schutte, A., Fraeman, A., Bhagwat, R., T. "Design Considerations for a Mars Highland Helicopter," Presented at the AIAA Ascend Conference, Virtual, November 16–18, 2020. https://rotorcraft.arc.nasa.gov/Publications/files/Mars_Highlands_Helicopter_AIAA_ASCEND_Final.pdf
44. Withrow–Maser, S., Johnson W., Young L., Koning, W., Kuang, W., Malpica C., Balaram J., Tzanetos, T., "Mars Science Helicopter: Conceptual Design of the Next Generation of Mars Rotorcraft," Presented at the AIAA Ascend Conference, Virtual, November 16–18, 2020. https://rotorcraft.arc.nasa.gov/Publications/files/MSH_summary_AIAA_ASCEND_final.pdf
45. Withrow-Maser, S., Koning W., Kuang W., Johnson, W., "Recent Efforts Enabling Future Mars Rotorcraft Missions," Presented at the VFS Aeromechanics for Advanced Vertical Flight Technical Meeting, San Jose, CA, January 21–23, 2020. https://rotorcraft.arc.nasa.gov/Publications/files/Shannah_Withrow_TVF_2020.pdf
46. Johnson, W., Withrow-Maser, S., Young, L., Malpica, C., Koning, W.J.F., Kuang, W., Fehler, M., Tuano, A., Chan, A., Datta, A., Chi, C., Lumba, R., Escobar, D., Balaram, J., Tzanetos, T., Grip, H., "Mars Science Helicopter Conceptual Design," NASA/TM–2020–220485. https://rotorcraft.arc.nasa.gov/Publications/files/MSH_WJohnson_TM2020rev.pdf
47. Johnson, W., "Mars Science Helicopter Mid-Year Review," Presented at NASA Jet Propulsion Laboratory, Pasadena, CA, March, 2020. https://rotorcraft.arc.nasa.gov/Publications/files/MSH_ARC_MYR_Mar2020rev.pdf
48. Coleman, C.P., "A Survey of Theoretical and Experimental Coaxial Rotor Aerodynamic Research," NASA TP-3675, March 1997.
49. Defauw, S., "Urban Air Mobility: a future alternative to current public transport," Solar Impulse Foundation, Aug. 2021. https://solarimpulse.com/news/urban-air-mobility-a-future-alternative-to-current-public-transport
50. NASA Langley Research Center, "Rotors for Mission to Titan Tested at Langley's Transonic Dynamics Tunnel," December 2022. https://www.nasa.gov/feature/langley/rotors-for-mission-to-titan-tested-at-langley-s-transonic-dynamics-tunnel
51. Cornelius, J., Schmitz, S., "Rotor Performance Predictions for UAM – Single vs Coaxial Rigid Rotors," The VFS Aeromechanics for Advanced Vertical Flight Technical Meeting, San Jose, CA, January 25-27, 2022. https://rotorcraft.arc.nasa.gov/Publications/files/Jason_Cornelius_Schmitz_12-Jan-22.pdf
52. Marshall, M., Tang, E., Cornelius, J., Ruiz, F., Schmitz, S., "Performance of the Dragonfly Lander's Coaxial Rotor in Vortex Ring State," AIAA SciTech Forum, AIAA 2024-0247, Miami, FL, Jan. 2024. https://doi.org/10.2514/6.2024-0247
53. Cornelius, J., Schmitz, S., Kinzel, M., "Efficient Computational Fluid Dynamics Approach for Coaxial Rotor Simulations in Hover," *AIAA Journal of Aircraft*, Vol. 58, No. 1, Jan. 2021. https://doi.org/10.2514/1.C036037
54. Kinzel, M., Cornelius, J., Schmitz, S., Palacios, J., Langelaan, J., Adams, D., Lorenz, R., "An Investigation of the Behavior of a Coaxial Rotor in Descent and Ground Effect," AIAA SciTech Forum, San Diego, CA, Jan. 7-11, 2019. https://doi.org/10.2514/6.2019-1098
55. Cornelius, J., Zhang, J., Schmitz, S., Smith, E., "Comprehensive Analysis of Coaxial Rotor Dynamics on a Support Arm," AIAA SciTech Forum, San Diego, CA, Jan. 3-7, 2022. https://doi.org/10.2514/6.2022-0930
56. Sukra Helitek, RotCFD: Rotor Computational Fluid Dynamics Integrated Design Environment, Software Package, Ver. 0.9.15 Build 402, Ames, IA, 2020. http://sukra-helitek.com/
57. Rajagopalan, G., Baskaran, V., Hollingsworth, A., Lestari, A., Garrick, D., Solis, E., and Hagerty, B., "RotCFD – A Tool for Aerodynamic Interference of Rotors: Validation and Capabilities," AHS Future Vertical Lift Aircraft Design Conference, San Francisco CA, Jan. 2012. https://rotorcraft.arc.nasa.gov/Publications/files/A-5-D_rajagopalan.pdf
58. Conley, S., Russell C., Kallstrom K., Koning W., Romander E., "Comparing RotCFD Predictions of the Multirotor Test Bed with Experimental Results," VFS 76th Annual Forum, Oct. 2020. https://rotorcraft.arc.nasa.gov/Publications/files/1429_Conley_070720.pdf
59. Rajagopalan, G., Thistle, J., and Polzin, W., "The Potential of GPU Computing for Design in RotCFD," AHS Technical Meeting on Aeromechanics Design for Transformative Vertical Lift, San Francisco, CA, Jan. 2018. https://rotorcraft.arc.nasa.gov/Publications/files/Rajagopalan_2018_TechMx.pdf
60. Mathur, S. R., and Murthy, J. Y., "A Pressure-based Method for Unstructured Meshes," *Journal of Numerical Heat Transfer*, Vol. 31, No. 2, pp. 195-215. https://doi.org/10.1080/10407799708915105
61. Sukra Helitek, AFTGen Airfoil Table Generator, Software Version 0.10.2, Ames, IA, Jan. 2022. http://sukra-helitek.com/
62. Koning, W., "Wind Tunnel Interference Effects on Tiltrotor Testing Using Computational Fluid Dynamics, NASA/CR-2016-219086, Mach, 2016. https://ntrs.nasa.gov/citations/20170000663
63. Cornelius, J., Schmitz, S., "Massive Graphical Processing Unit Parallelization for Multirotor

Computational Fluid Dynamics," *AIAA Journal of Aircraft*, Vol. 60, No. 6, Nov. 2023. https://doi.org/10.2514/1.C037356

64. Johnson, W., "Model for Vortexs Ring State Influence on Rotorcraft Flight Dynamics," NASA/TP-2005-213477, Dec. 2005. https://ntrs.nasa.gov/citations/20060024029
65. Cornelius, J., "Designing a Coaxial Quadrotor for Urban Air Mobility," VFS Autonomous VTOL Technical Meeting, Mesa, AZ, Jan. 24-26, 2023. https://ntrs.nasa.gov/api/citations/20230000666/downloads/1602_Cornelius_011323.pdf